Contents lists available at ScienceDirect

Arabian Journal of Chemistry

journal homepage: www.ksu.edu.sa

Original article

Photothermal-triggered release of alkyl radicals hydrogel via versatile carbon dots chelating Ag^{+} and its synergistic anti-bacterial and biofilm activities

Wen Liu [a,b,d,*], Baizhi Su [b], Hua Song [b], Xueyun Zhang [b], Guodong Ren [b], Xuewei Wang [b], Lili Yan [b,d], Sufang Ma [b], Lihong Li [b,d], Lixia Guo [c], Shuming Xu [e], Boye Zhang [b], Haipeng Diao [b,d,*], Zhifang Wu [a], Sijin Li [a], Chengwu Zhang [b]

[a] The First Hospital of Shanxi Medical University, The First Clinical Medical School of Shanxi Medical University, Taiyuan 030001, PR China
[b] School of Basic Medical Sciences, Shanxi Medical University, Taiyuan 030001, PR China
[c] College of Pharmacy, Shanxi Medical University, Taiyuan 030001, PR China
[d] Key Laboratory of Cellular Physiology at Shanxi Medical University, Ministry of Education, Taiyuan 030001, PR China
[e] Women Health Center of Shanxi, Taiyuan 030013, PR China

ARTICLE INFO

Keywords:
Carbon dots
Hydrogel
Photothermal
Alkyl radical
Bacterial biofilm

ABSTRACT

Staphylococcus aureus has become one of the most common pathogens in clinical tissue infection, and it is easy to form biofilm. Incomplete removal of biofilms often leads to recurrent infections, and more serious is the possibility of bacteria developing drug resistance. Therefore, the effective eradication of refractory biofilms is essential. Herein, a temperature-sensitive hydrogel was prepared by doping the photothermal carbon dots (PTCDs) chelated by Ag^{+}, and the AIPH which could produce alkyl radicals in response to heat into the thermodissolved gelatin. Under the irradiation of 660 nm laser, the PTCDs generated heat to dissolve the hydrogel, and promoted chelation of silver ions in PTCDs for chemical sterilization. Meanwhile, the heat generated by the PTCDs induced the 2,2′-azobis[2-(2-imidazolin-2-yl) propane] dihydrochloride (AIPH) to produce alkyl free radical sterilization, achieving the purpose of photothermal/thermodynamic/chemical synergistic to kill *Staphylococci aureus* and destroy its biofilm. Therefore, the biocompatible PTCDs@Ag-AIPH hydrogel proposed in this study was a promising composite that could eliminate biofilms and promoted wound healing, showing good potential in future biomedical applications.

1. Introduction

Bacterial infections can cause serious diseases such as endocarditis, meningitis, pneumonia, etc., which are serious worldwide threat to human health (Rello et al., 2019; Bastien et al., 2023; Dong et al., 2020; Jin et al., 2024). A report by the World Health Organization (WHO) highlights that around 700,000 people die from multidrug-resistant bacteria (MDR) globally each year, and this number is expected to grow to 10 million by 2050 (Willyard et al., 2017; Kawabe et al., 2022). Antibiotics are currently accepted as the main treatment for bacterial infections. However, overuse of antibiotics has led to resistance, which reduces the success rate of conventional antibiotic treatment and leads to the spread of resistant pathogens (Nies et al., 2023; Chen et al., 2024). In addition, the presence of biofilms makes it difficult to destroy bacteria at the site of infection. Biofilm is a colony of bacteria gathered together, which irreversibly attach to the surface of living or non-living carriers and are encapsulated in self-produced polymeric substances (such as exopolysaccharides, enzymes, bacterial DNA and proteins), which is a haven for bacteria to survive and reproduce, and communicate with each other through quorum sensing (Dieltjens et al., 2020; Wan et al., 2023; Mukherjee et al., 2019). Antibiotic treatment usually resolves symptoms caused by bacteria, but it is difficult to eradicate both the bacteria embedded in the biofilm and the biofilm itself because the protection of the biofilm matrix against the bacteria increases their resistance to antibiotics by 10 to 1000 times (Rumbaugh et al., 2020; Mah et al., 2001; Liu et al., 2022a). *Staphylococcus aureus* (*S. aureus*) has

* Corresponding authors at: The First Hospital of Shanxi Medical University, The First Clinical Medical School of Shanxi Medical University, Taiyuan 030001, PR China (Wen Liu); School of Basic Medical Sciences, Shanxi Medical University, Taiyuan 030001, PR China (Haipeng Diao).
E-mail addresses: liuwen@sxmu.edu.cn (W. Liu), diaohp@sxmu.edu.cn (H. Diao).

https://doi.org/10.1016/j.arabjc.2024.105755
Received 26 February 2024; Accepted 23 March 2024
Available online 24 March 2024

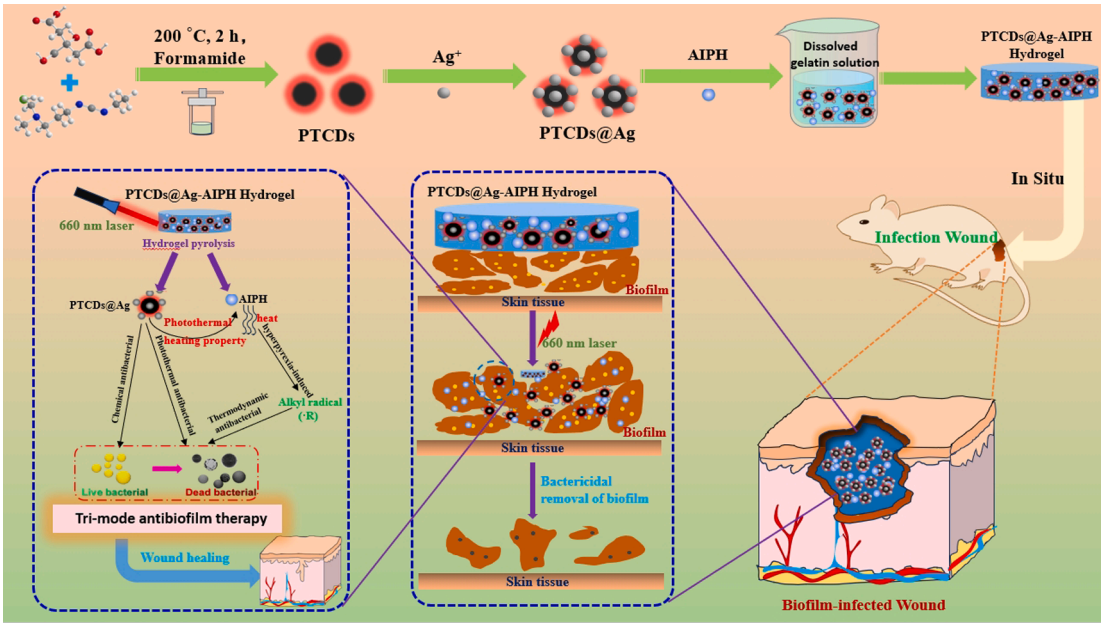

Scheme 1. Schematic illustration for the synthesis of photothermal-triggered release of alkyl radicals hydrogel (PTCDs@Ag-AIPH Hydrogel) and its synergistic antibacterial and biofilm activities *in vivo*.

become one of the most common pathogens in clinical tissue infection, and it is easy to form biofilms, which makes it more difficult to destroy the bacteria at the infected site (Shan et al., 2024).

As a kind of carbon nanomaterials with great potential, carbon dots (CDs) have attracted wide attention since its discovery in 2004. CDs are typical quasi-spherical nanoparticles with average size of less than 10 nm. CDs have the advantages of small particle size, fluorescence, good biocompatibility, and hydrophilicity (Ren et al., 2022; Liu et al., 2022b; Yang et al., 2023; Nugroho et al., 2024). The antibacterial performance of CDs depends on the core properties of nanomaterials, especially the functional groups and the charges expose on the CDs surface. Currently reported antibacterial CDs mainly rely on retaining bacteriostatic groups of synthetic raw materials to achieve sterilization effect: for example, CDs prepared from turmeric leaves by hydrothermal method can effectively eradicate *Klebsiella pneumoniae*, *Staphylococcus*, *Escherichia coli* and *S. aureus* (Song et al., 2018). Some CDs were antibacterial by producing ROS. For example, the mixture of bacteria and EDA CDs was exposed to visible light for 6 h, and there was significant difference between the light treatment and the control group (Das et al., 2018). However, there are some defects in the carbon dots used for bacteriostasis, such as few types, short fluorescence emission wavelength, single performance and long irradiation time, etc. Photothermal therapy (PTT) is a non-invasive treatment based on the conversion of photons into heat energy, which makes proteins qualitative and enzymatic degeneration leads to irreversible bacterial damage resulting in destruction of pathogens (Shen et al., 2023; Rajasekar et al., 2020). Photothermal bactericidal therapy has attracted more and more attention because of its high efficiency and its ability to reduce the occurrence of drug resistance of pathogenic bacteria. Many nanomaterials have been studied as photothermal agents, which can convert light energy into heat energy for sterilization, and can further trigger the release of drugs. Such nanomaterials show excellent photostability, low cost and high photothermal conversion efficiency, but there are some problems such as poor solubility and large particle size, and the high temperature generated by the photothermal sterilization process will damage the surrounding normal tissues. CDs as a nanomaterial with small size and uniform particle size, can overcome these disadvantages of poor solubility and large size. Its good photothermal properties and photothermal conversion ability are now widely used in tumor therapy as well as bacterial sterilization (Geng et al., 2023). However, PTT alone is not effective in killing resistant bacteria. Therefore, thermotherapy can inactivate the bioactive matrix inherent in the biofilm, destroy the structure of the biofilm, and together with other antibacterial strategies, will be more effective in eliminating bacteria.

Some metal ions, such as Ag^{+}, Cu^{2+}, Fe^{3+}, Mn^{2+}, etc., have strong antibacterial or promoting wound healing ability. By destroying the function of the bacterial cell membrane, they enter the bacterial interior, interfere with the bacterial metabolic process, and make some bacterial contents escape, resulting in the death of bacteria. Alkyl free radical (·R) is a kind of free radical, independent of O_2 level, which can directly oxidize bacterial components or induce oxidative stress, providing another option for the removal of biofilm bacteria under hypoxia conditions, ·R is easily produced by thermal decomposition of azo compounds (Yu et al., 2019; Lin et al., 2022; Wang et al., 2020; Li et al., 2023). However, high concentration of metal ions in the body has greater toxic and side effects, it is important to strictly control the concentration of theirs use. Single treatment has the defect of incomplete killing of bacteria. In order to solve the above issues, it is very necessary to design and construct a new type of nanomedicine that can kill bacteria safely and efficiently.

As a delivery carrier, hydrogels have a wide range of applications due to their multifunctional integration and can help wounds heal faster by keeping them moist. The water absorption capacity of hydrogels is beneficial to absorb wound exudates, accelerate wound healing process and reduce infection rate (Sun et al., 2006; Bao et al., 2011; Cui et al., 2023). Gelatin as a commonly used material for hydrogels has many advantages, such as swelling capacity, biodegradability, biocompatibility, etc. And gelatin gel formation is mainly caused by its intermolecular interactions and the interactions between protein components and water molecules. It provides an excellent basis for the function of each part of the composite material (Stubbe et al., 2021; Lu et al., 2022). Besides, hydrogels have many advantages and thus widely used in the biomedical field (Long et al., 2023; Zhao et al., 2023; Zhou et al., 2023; He et al., 2022; Maria et al., 2023). However, the preparation of most hydrogels requires crosslinking of various materials in appropriate proportions, which is expensive and complicated. The development of a multifunctional nanodrug that uses multiple synergistic therapies to promote sterilization and eradication of the resulting biofilm while

reducing its adverse side effects.

Herein, a novel multifunctional hydrogel (PTCDs@Ag-AIPH Hydrogel) was successfully constructed and used for bacterial killing and wound healing (Scheme 1). Among them, CDs with red fluorescence emission and photothermal properties (PTCDs) were synthesized by solvothermal method, using 1-(3-dimethylaminopropyl)-3-ethylcarbodiimide hydrochloride and citric acid as raw materials and formamide as reaction solvent. The PTCDs were chelated with Ag^+ and co-loaded with AIPH with thermodynamic properties in the hydrogel prepared by gelatin, so as to prepare a heat-activated hydrogel sterilization system (PTCDs@Ag-AIPH Hydrogel). After injection into the wound site, the hydrogel rapidly gels with the decrease of temperature. Under 660 nm laser light, the PTCDs generated heat to dissolve the hydrogel and release Ag^+ sterilization. Meanwhile, the heat generated by the PTCDs promoted the production of alkyl free radical sterilization of AIPH, so as to achieve the goal of photothermal/thermodynamic/chemical synergistic killing of *S. aureus* and destruction of its biofilm. The bactericidal activity of multifunctional hydrogels was confirmed with remarkable killing effect on *S. aureus* and its biofilm *in vivo* and *in vitro*.

2. Experimental sections

2.1. Materials and reagents

Citric acid, formamide, gelatin and all metallic salts were purchased from the Aladdin Biochemical Technology Co., Ltd. (Shanghai, China). Azodiisobulimidazoline hydrochloride (AIPH) was purchased from the Tokyo Chemical Industry (Tokyo, Japan). 1-(3-dimethylaminopropyl)-3-ethylcarbodiimide hydrochloride, 3-(4,5-dimethylthiazol-2-yl)-2,5-diphenyltetrazole bromide, 2,2′-Azino-bis(3-ethylbenzothiazoline-6-sulfonic acid) diammonium salt (ABTS), Calcein-AM/PI live cell/dead cell double staining kit (Calcein-AM/PI) and Hematoxylin-Eosin (H&E) stain Kit were purchased from Solarbio Science & Technology Co., Ltd. (Beijing, China).

2.2. Preparation, characterization and optical properties of PTCDs

The citric acid and 1-(3-dimethylaminopropyl)-3-ethylcarbodiimide hydrochloride were dissolved in formamide and transferred to a high-pressure reactor at the right temperature and reaction time. After that, the solution was kept at room temperature for cooling down and centrifuged at 10000 rpm for 10 min. The supernatant was collected and filtered by a 0.22 μm microporous filter. After the large particles were removed, they were dialyzed with a molecular weight of 1000 Da for 24 h and lyophilized. The dark red PTCDs powder obtained. The optimum synthesis conditions were studied, included synthesis time, the mass ratio of raw material, and the reaction temperature. The morphology and particle size of PTCDs were characterized by transmission electron microscopy (TEM, Tecnai G2 F20, FEI, America), the size of 50 PTCDs was measured on the obtained image, and the particle size statistical map was drawn. The thickness of PTCDs was characterized by atomic force microscopy (AFM, Dimension Icon, Bruker, Germany). The carbon structure of PTCDs was characterized by X-ray diffraction (XRD, D8 Advance, Bruker, Germany) instrument. The elemental composition and chemical bond of PTCDs were characterized by X-ray energy spectroscopy (XPS, Escalab 250Xi, Thermo, America). Surface functional groups of PTCDs were characterized by Fourier transform infrared spectroscopy (FTIR, INVENIO, Bruker, Germany).

The optical properties of PTCDs were determined by UV–Vis spectrophotometer (UV–Vis, UH5300, Hitachi, Japan) and fluorescence spectrophotometer (F7100, Hitachi, Japan). 0.10 mg/mL of PTCDs solution was placed in a quartz colorimetric dish and fluorescence was measured in a fluorescence spectrophotometer. The slits of Ex and Em were set to 10 nm, and different excitation wavelengths were set for determination to determine the best excitation wavelength and the best emission wavelength. In addition, the effects of different ionic strength, pH and storage time on the fluorescence properties of PTCDs were studied. The effects of different metal ions on PTCDs fluorescence and the sensitive response to silver ions were studied.

The photothermal properties of PTCDs had also been studied. The photothermal properties of PTCDs under different irradiation times are as follows: PTCDs were prepared into solutions with concentrations of 0.20 mg/mL, 0.30 mg/mL and 0.40 mg/mL, and 200 μL was irradiated in an EP tube for 15 min under 660 nm laser, and the temperature change was measured. The real-time infrared thermal imager was used to take pictures. The photothermal properties of PTCDs under different power laser irradiation. The PTCDs was prepared into a solution with a concentration of 0.30 mg/mL, the 660 nm laser was irradiated at different optical power densities (0.50 W/cm^2, 1.0 W/cm^2, 1.5 W/cm^2) for 15 min, and the temperature changes were measured and recorded by a real-time infrared thermal imager. Photothermal heating stability of PTCDs was measured. The PTCDs was prepared into a solution with a concentration of 0.30 mg/mL, and irradiated with a 660 nm laser at a power density of 1.0 W/cm^2 for 15 min, and then the laser irradiation was stopped and cooled at room temperature for 15 min. Start the laser irradiation again, cycle 5 times, and test the temperature change with the temperature detector.

2.3. Preparation, characterization and properties of PTCDs@Ag-AIPH Hydrogel

A certain amount of gelatin was weighed and dissolved in water and placed in an oven at 65 ℃ to dissolve slowly. The gelatin was prepared as 40 μg/mL blank hydrogel, and doped with carbon dots complex PTCDs@Ag and AIPH which released alkyl radicals in response to temperature at room temperature ([PTCDs] = 0.30 mg/mL, [Ag^+] = 1.2 μg/mL, [AIPH] = 0.80 mg/mL). The PTCDs@Ag-AIPH Hydrogel is obtained. The morphologies of blank Hydrogel and composite Hydrogel (PTCDs@Ag-AIPH Hydrogel) were characterized by high-resolution scanning electron microscopy (SEM, JSM-6701F, JEOL, Japan). The hydrogels were freeze-dried, and the same size were cut respectively and placed in ultra-pure water. The swelling rate of the hydrogels were measured by weighing them every 30 min.

2.4. Cell cytotoxicity in vitro

In order to study the biocompatibility of PTCDs and PTCDs@Ag-AIPH Hydrogel, human normal cervical epithelium (HcerEpic) cells were used as template cells to determine the cytotoxicity of PTCDs and Hydrogels by MTT assay. First, HcerEpic cells in the logarithmic growth stage were inoculated into 96-well plates and cultured in cell incubator for 24 h. After discarding the culture medium, different concentrations PTCDs and Hydrogel solutions were prepared with DMEM culture medium and 100 μL per well was added into 96-well plates for 24 h. The different groups (Hydrogel, PTCDs Hydrogel, PTCDs-AIPH Hydrogel, AIPH Hydrogel, PTCDs@Ag-AIPH Hydrogel, [PTCDs] = 0.30 mg/mL, [Ag^+] = 1.2 μg/mL, [AIPH] = 0.80 mg/mL) were added in the corresponding wells. The culture medium was discarded, and 100 μL MTT (0.50 mg/mL) was added for further incubation for 4 h. The absorption value at 490 nm was detected.

2.5. Antibacterial and antibiofilm activity in vitro

The antibacterial properties of different Hydrogels were evaluated using *S. aureus* cultivated in nutrient broth (NB) at 37 °C for 10 h. The bacteria count was about 1×10^6 CFU/mL before the experiment began. The 25 μL bacteria suspensions were divided into different groups (Hydrogel, PTCDs Hydrogel, PTCDs-AIPH Hydrogel, PTCDs@Ag Hydrogel, PTCDs@Ag-AIPH Hydrogel, [PTCDs] = 0.10 mg/mL, [Ag^+] = 0.60 μg/mL, [AIPH] = 0.20 mg/mL) to 100 μL mixed bacteria suspensions and incubated in an incubator at 37 ℃ for 20 min. The laser groups were exposed under a 660 nm laser (1.0 W/cm^2) for 20 min. The

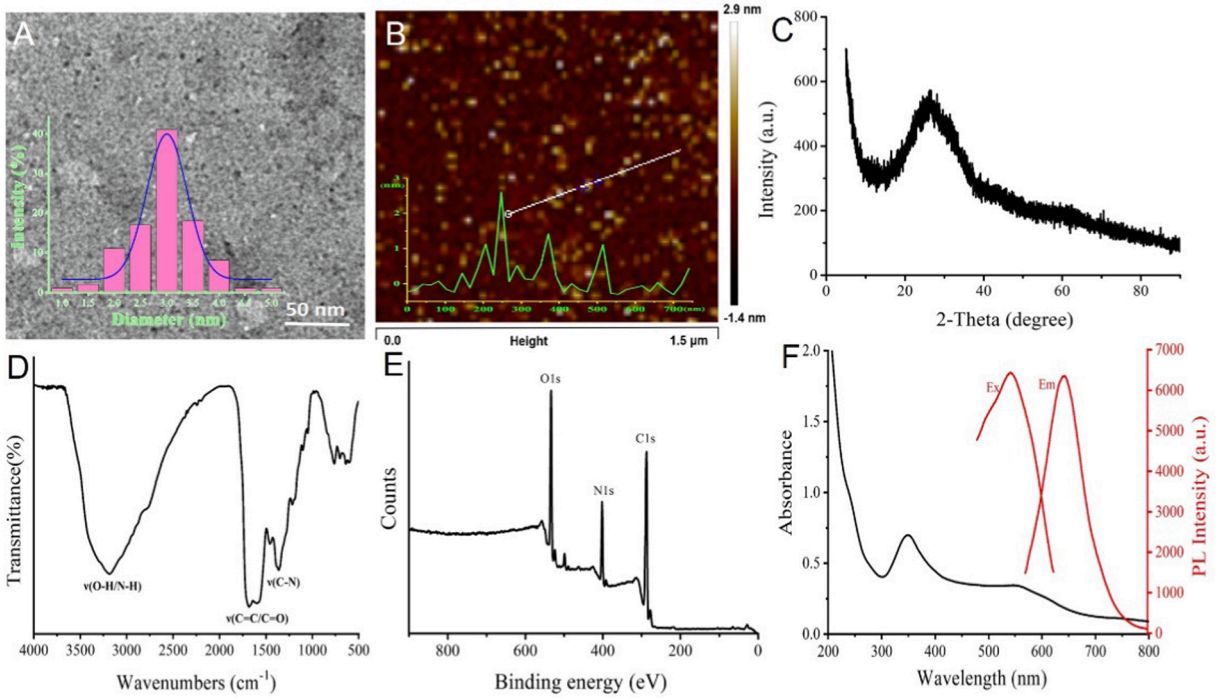

Fig. 1. (A) TEM diagram of PTCDs (inset: diameter distribution of PTCDs, scale bar is 50 nm); (B) AFM image of PTCDs (inset: height profile of PTCDs); (C) XRD pattern of PTCDs; (D) FT-IR spectrum of PTCDs; (E) XPS spectrum of PTCDs; (F) The UV–Visible absorption spectrum, best excitation spectrum and best emission spectrum of PTCDs.

standard continuous dilution method was used to quantified the number of viable bacteria in each group. The 100 μL last bacterial solutions were spread on agar plates and cultured for 12 h. The colonies were counted and the survival rate was calculated.

In order to better simulate the wound environment after infection *in vivo*, that is, bacteria form self-protecting biofilm, we first simulated the formation of bacterial biofilm *in vitro* and studied the killing of Hydrogels on it. A 96-well plate was taken, and the bacterial solution (5×10^7 CFU/mL) was diluted 10 times with TSB medium containing 1 % glucose, 100 μL was added to each well, and cultured at 37 ℃ for 24 h, *S. aureus* biofilm was formed at the bottom of the well. The different groups (Hydrogel, PTCDs Hydrogel, PTCDs-AIPH Hydrogel, PTCDs@Ag Hydrogel, PTCDs@Ag-AIPH Hydrogel, [PTCDs] = 0.30 mg/mL, [Ag^+] = 1.2 μg/mL, [AIPH] = 0.80 mg/mL) were added in the corresponding wells and incubated in an incubator at 37 ℃ for 20 min. The different groups were divided into laser irradiation (660 nm, 1.0 W/cm^2) for 20 min or no laser irradiation, and incubated for 12 h. The survival rate of *S. aureus* was calculated.

In addition, in order to more directly observe the antibacterial properties, the different Hydrogel groups were studied by staining of SYTO 9 (0.10 μM, live bacteria, green fluorescence) and PI (50 μg/mL, dead bacteria, red fluorescence) under confocal laser scanning microscopy (CLSM). The morphologies of *S. aureus* and its biofilm were observed by scanning electron microscope (SEM) before and after treated to PTCDs@Ag-AIPH Hydrogel. Meanwhile, in order to prove the successful preparation of *S. aureus* biofilm and verify the killing effect of different hydrogels on the biofilm, The formed biofilm was crystal violet for 15 min and photographed.

2.6. Anti-infection assays in vivo

This experiment was approved by the Animal Ethics and Use Committee of Shanxi Medical University (License Number: 2019–0009). The BALB/c mice used in the experiment were all provided by the Animal Experimental Center of Shanxi Medical University, aged 6 weeks and weighing 15 g ± 1 g/mouse. Mice in groups of two were placed in non-toxic cages in an air-conditioned room at room temperature of 22 °C, fed with SPF full value nutritional pellets and sterile water, and the bedding material was changed for 2–3 days. Before wound modeling, the leukocyte reduction was induced by cyclophosphamide at 100 μg/kg per mouse on day 1 and day 3. After induction, the leukocyte values of the mice and normal uninduced mice were examined by orbital blood sampling with EDTA anticoagulant tube.

Isoflurane anesthesia was used, back hair was removed, the skin inside the circle with a diameter of 6 mm was cut off, and 20 μL of 100 μL of *S. aureus* bacteria (2×10^8 CFU/mL) was inoculated into the fresh mouse wound tissues and cultured to form wound abscess, causing the wound to form a biofilm infection. The mice were randomly divided into four groups, namely Hydrogel, Hydrogel + Laser, PTCDs@Ag-AIPH Hydrogel, PTCDs@Ag-AIPH Hydrogel + Laser, with 5 mice in each group, and were treated once every two days. In the plus laser group, the wound was irradiated with 660 nm laser (1.0 W/cm^2) for 15 min, and the wound was photographed every 4 days. The photothermal imaging of composite hydrogel and laser was performed, and the blank hydrogel group was used as the control. The mice were anesthetized and evenly applied different hydrogels to the wound sites, and irradiated with a 660 nm laser for 15 min, recorded its temperature change every minute, and took pictures with an infrared thermal imager every 3 min. The mice were euthanized, the wound tissues of each group were dissected, cut with sterile instruments, placed in 10 mL NB culture medium, shaken in a shaking table for 10 h, bacterial culture was performed, and colonies were counted. At the same time, to assess the safety of the composite hydrogel, the major organs and wound tissues of some mice in the anatomical experimental group and the blank group were fixed in 4 % paraformaldehyde, sliced, and photographed under the microscope after H&E staining.

3. Results and discussion

3.1. Preparation and characterization of PTCDs

In order to optimize the optical properties of PTCDs, as shown in

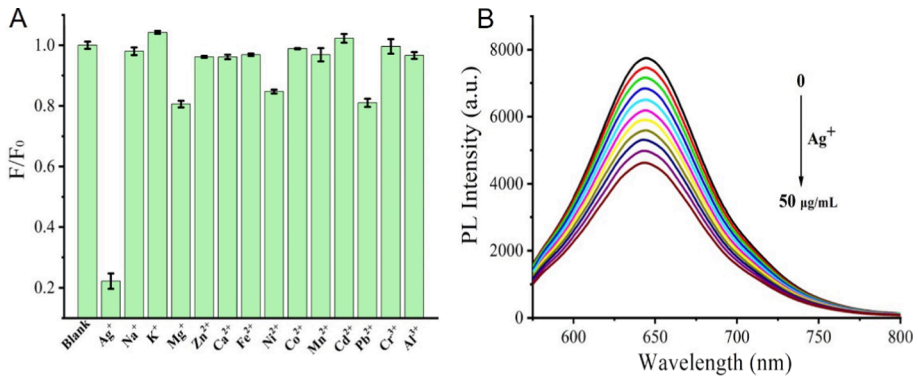

Fig. 2. (A) F/F_0 of PTCDs in the presence of various metal ions; (B) The fluorescence emission spectra changes of PTCDs with different concentrations of Ag^+ (Ex = 550 nm).

Fig. S1, the reaction time, reaction temperature and mass ratio of synthetic raw materials were studied respectively. The results showed that the optimum reaction conditions were reaction time of 2 h, mass ratio of reactant 5:1 (citric acid:1-(3-dimethylaminopropyl)-3-ethylcarbodiimide hydrochloride), reaction temperature of 200 ℃.

In Fig. 1A, the morphology and particle size of PTCDs were characterized by HR-TEM. TEM images showed that PTCDs were quasi-spherical nanoparticles with uniform distribution, and the average diameter of PTCDs was 3 nm. In Fig. 1B, the height of PTCDs was characterized by AFM, which showed that the average height of PTCDs was about 2.9 nm, which was consistent with TEM results, further indicating that PTCDs were spherical carbon dots with small particle size. As shown in Fig. 1C, the crystal structure of PTCDs was characterized by XRD with a wide diffraction center of 25° (2θ = 25°), which was attributed to the D-spacing of the graphitic carbon plane, indicating that PTCDs were mainly composed of amorphous carbon (Liu et al., 2022b). FTIR was used to characterize the surface functional groups of PTCDs. The results were shown in Fig. 1D. There was a wide shoulder peak at 3430 cm^{-1}, which could be attributed to the stretching vibration of O–H and N–H. The absorption band at 1623 cm^{-1} is attributed to stretching vibrations of C = C or C = O; 1405 cm^{-1} can be attributed to the bending vibration of C-N, indicating that the surface of PTCDs contains hydrophilic groups such as hydroxyl, carboxyl and amino groups (Liu et al., 2022b; Ren et al., 2022). The chemical composition of PTCDs was characterized by XPS. Fig. 1(E) showed that PTCDs had three distinct binding energy peaks, namely C1s (287.6 eV),

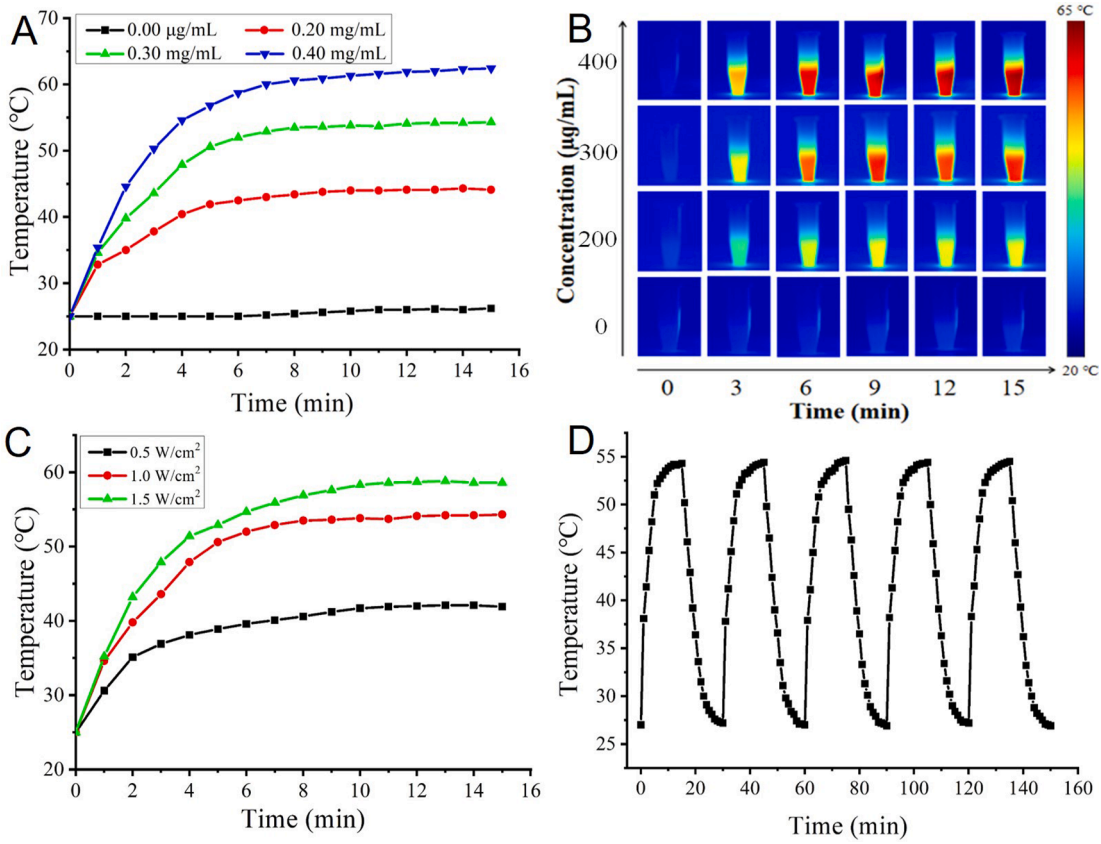

Fig. 3. (A) Temperature dependence of laser-irradiated for different concentration of PTCDs as a function of irradiation time; (B) Thermal images of PTCDs dispersions with different concentrations and irradiation times; (C) Photothermal curves of PTCDs (300 μg/mL) under laser irradiation with various power densities; (D) Photothermal heating stability of PTCDs.

N1s (403.6 eV) and O1s (535.0 eV), indicating the presence of carbon, nitrogen and oxygen. The surface functional groups of PTCDs were analyzed by high-resolution XPS spectroscopy. Fig. S2A showed the high-resolution C1s scans of PTCDs, with four peaks at 284.6, 285.9, 287.5 and 288.7 eV, which can be attributed to C = C/C–C, C-N, C-O, C = O, respectively. Fig. S2B showed the high-resolution N1s scans of PTCDs, the two peaks of 398.8 and 399.9 eV corresponded to C-N-C and N–H, respectively. Fig. S2C showed the high-resolution O1s scans of PTCDs, there were two signals 531.0 and 532.3 eV, which could be attributed to C = O and C-OH /C-O-C, respectively (Ren et al., 2022). High resolution XPS showed that PTCDs contained amino, hydroxyl, carboxyl and other functional groups, which was consistent with FTIR results.

3.2. Optical properties of PTCDs

The optical properties of the PTCDs were also determined. In Fig. 1F, the black line showed the UV–visible absorption spectrum of PTCDs with absorption peaks at 350 nm and 550 nm, while the red line showed the optimal excitation (Ex) and emission spectrum (Em) with the optimal Ex wavelength at 550 nm and the optimal Em wavelength at 645 nm. Fig. S3A showed the fluorescence emission spectra of PTCDs at different excitation wavelengths ranges from 520 to 580 nm, the fluorescence intensity at 645 nm was the strongest when excitation wavelength located at 550 nm. The optical stability of PTCDs was investigated. It can be seen from the Fig. S3B that the fluorescence of PTCDs did not change significantly even if the concentration of NaCl reached 3.0 M. Fig. S3C showed the fluorescence intensity changes of PTCDs under different pH buffer solutions. The results showed that the fluorescence intensity of PTCDs was stable between pH 4–10. Fig. S3D showed the change of fluorescence intensity of PTCDs with the storage time for 30 d, the fluorescence intensity still did not decrease significantly, indicating that PTCDs had excellent luminescence stability.

Due to the abundant heteroatoms on the surface of PTCDs, the chelating metal ion provides a favorable action site and a target to endow carbon dots with new properties. Therefore, the chelation of PTCDs with different metal ions was investigated. As seen in Fig. 2A, among the various analytes (e.g., Ag^{+}, Na^{+}, K^{+}, Mg^{2+}, Zn^{2+}, Ca^{2+}, Fe^{2+}, Ni^{2+}, Co^{2+}, Mn^{2+}, Cd^{2+}, Pb^{2+}, Cr^{3+} and Al^{3+}), Ag^{+} caused the fluorescence quenching of PTCDs, which indicated its excellent selectivity for Ag^{+}. To examine the dose-dependent response of PTCDs to Ag^{+}, different amounts of Ag^{+} were reacted with PTCDs of the same concentration. As shown in Fig. 2B, detailed fluorescence titration was performed at the excitation wavelength of 550 nm. With the increase of Ag^{+} concentration, the intensity of emission band at 645 nm decreased gradually, indicating that Ag^{+} reacted with the PTCDs. To further assess the chelating effect between PTCDs and Ag^{+}, the absorbance spectrum of mixture of PTCDs and Ag^{+} were tested and recorded. As shown in Fig. S4, with the concentration of silver ions increasing, the peak at 350 nm gradually rised, which could be attributed to formation of spherical silver nanoparticles by the combination of Ag^{+} and carbon dots (Jin et al., 2018). Ag^{+} has better antibacterial properties, which will endow PTCDs with stronger synergistic antibacterial ability.

3.3. Photothermal properties of PTCDs

Fig. 3A showed the temperature changes of different concentrations of PTCDs (0, 0.20, 0.30 and 0.40 mg/mL) irradiated by laser at 660 nm and 1.0 W/cm^2 for different time periods. The control group showed no obvious temperature changes after laser irradiation, indicating that the control group had no photothermal conversion performance. The temperature of 0.20 mg/mL and 0.30 mg/mL PTCDs could reach 40 °C and 53 °C after irradiation 15 min, while the final temperature of 0.40 mg/mL PTCDs could reach 62 °C under the same conditions, indicating that the higher the concentration of PTCDs in a certain concentration range, the better the photothermal conversion performance. At the same time, the relative stability of temperature could be reached after 6 min irradiation. In Fig. 3B, the real-time infrared thermal imager was used to take photos and record the temperature changes of PTCDs solution with different concentrations in the process of laser irradiation, which further verified that PTCDs had good photothermal conversion performance. The photothermal properties of PTCDs (0.30 mg/mL) under different power laser irradiation were investigated. Fig. 3C showed the temperature variation curves of PTCDs under different laser power irradiation for 15 min. After 15 min irradiation with 660 nm laser power of 0.5 W/cm^2, 1.0 W/cm^2 and 1.5 W/cm^2, the solution temperature of PTCDs reached 41 °C, 53 °C and 58 °C, indicating that with the increase of 660 nm laser power density, the temperature of PTCDs solution increased more. In order to better display the photothermal conversion performance and photothermal stability of the synthesized PTCDs, PTCDs concentration of 0.30 mg/mL and laser power density of 1.0 W/cm^2 were selected for follow-up experiments. As shown in Fig. 3D, in the five cycles (laser switching cycle), the temperature curves of PTCDs were basically consistent, the maximum temperature of each cycle reached 54 °C. After being reduced to room temperature and laser irradiation, the photothermal conversion response was good, indicating that the prepared PTCDs had good photothermal conversion stability.

3.4. Release of alkyl radical of AIPH in vitro

Commercial probe ABTS were used to detect alkyl free radicals from AIPH under different conditions. As shown in Fig. S5A, with the increase of AIPH concentration, the amount of alkyl radicals produced by AIPH also linearly increased incubation in a water bath for 55 ℃. In Fig. S5B, the probe incubated with AIPH for different time at 55 ℃, with the extension of incubation time, the alkyl radical produced by AIPH gradually increased and reached a plateau for 30 min. Fig. S5C showed absorption curves of the probe at different temperatures in the presence and absence of AIPH, the results indicated that the release of alkyl radical increased after the probe reacted with AIPH with the increase of temperature. As seen in Fig. S5D, at different pH, the absorption curves of the probe itself and its interaction with alkyl radicals generated by AIPH. The release of alkyl radicals from AIPH was stable after incubation at the same temperature in the pH 4–11 range, the alkyl radicals produced by AIPH gradually increase with decreasing pH in the pH 1–4 range. The insets in Fig. S5 showed the color change of the solution before and after the alkyl radical probe interacted with the alkyl radical produced by AIPH, the darker the color, the more alkyl radicals produced. In conclusion, AIPH had good ability to release alkyl radicals under suitable conditions.

3.5. Preparation and properties determination of multifunctional thermal hydrogels

Hydrogels are gel states at room and low temperatures, but they become sol states at higher temperatures. Hydrogels in the gel and sol states were presented in Fig. S6A. The morphologies of Hydrogel and composite Hydrogel (PTCDs@Ag-AIPH Hydrogel) were characterized by HR-SEM, as shown in Fig. S6(B, C). The results showed that the prepared hydrogel had a porous structure, and the structure of hydrogel did not change significantly after the addition of PTCDs and AIPH. To evaluate their water absorption properties, the swelling rates of Hydrogel and composite Hydrogel (PTCDs@Ag-AIPH Hydrogel) were measured (place in ultra-pure water and weigh every 30 min). As shown in Fig. S6D, the swelling rates of Hydrogel and PTCDs@Ag-AIPH Hydrogel were 24 and 27 respectively at 6 h. It showed that the hydrogel had good water absorption ability and strong potential to absorb wound exudation. Moreover, the rheological properties of PTCDs@Ag-AIPH hydrogels were also tested. As showed in Fig. S6 (E, F), strain scan experiments showed that the hydrogel spots had a 100 % chance of fracturing, dynamic frequency scanning showed that the energy storage modulus was consistently higher than the loss modulus from 0.1 to 10 Hz, indicating

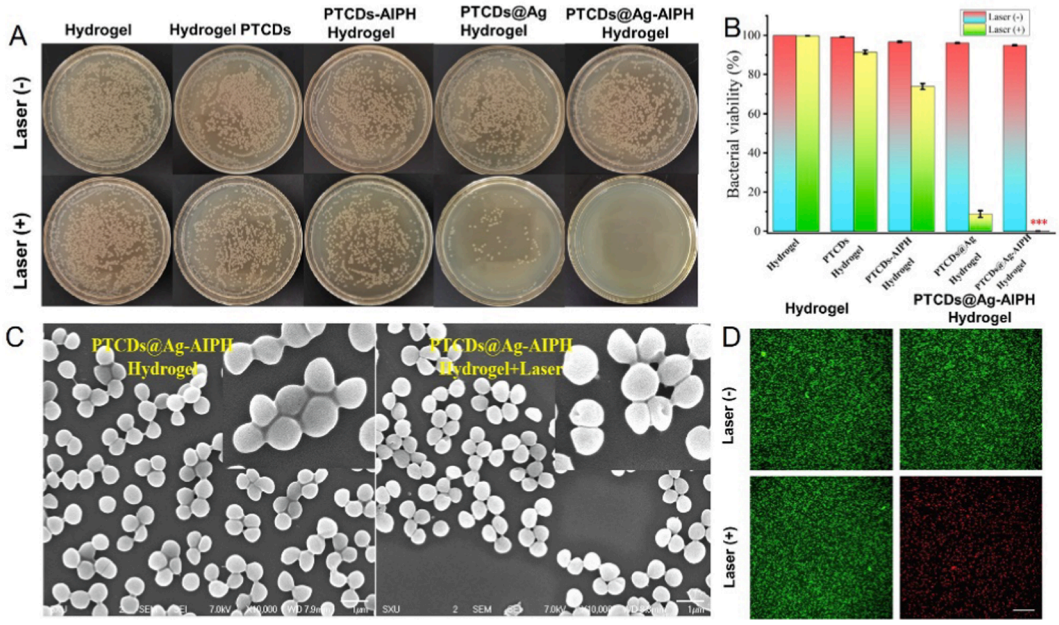

Fig. 4. (A) The plate photos of bacteria cocultured with different Hydrogel groups under 660 nm laser irradiation or not. The final bacteria suspension concentrations were adjusted to 10^6 CFU·mL^{-1}. (B) The viability rate of the different Hydrogels against *S. aureus* (***P < 0.001, *vs* Hydrogel group); (C) The SEM images of *S. aureus* cocultured with different Hydrogel groups. Scale bar = 1 μm; (D) The specific killing effects of *S. aureus* by live/dead staining. Scale bar = 20 μm.

that the hydrogel had good viscoelasticity.

3.6. Cytotoxicity test

The cytotoxicity of PTCDs and Hydrogels were evaluated by HcerEpic cells. In Fig. S7A, even when the concentration of PTCDs was as high as 900 μg/mL, the survival rate of cells was still more than 80 %, indicating that PTCDs had good biocompatibility. The cytotoxicity of Hydrogel, PTCDs@Ag Hydrogel, AIPH Hydrogel and PTCDs@Ag-AIPH Hydrogel to HcerEpic were studied. MTT test results were shown in Fig. S7B. After incubating with cells for 24 h, the cell survival rate of the final composite Hydrogel was still above 80 %, indicating that PTCDs@Ag-AIPH Hydrogel had good biocompatibility.

3.7. Antibacterial activity test

S. aureus was selected as the model bacteria for the antibacterial assays. We further explored the antimicrobial properties of the prepared composite hydrogels with and without laser irradiation. As shown in Fig. 4, the viabilities of *S. aureus* after being treated with Hydrogel, PTCDs Hydrogel, PTCDs-AIPH Hydrogel, PTCDs@Ag Hydrogel, PTCDs@Ag-AIPH Hydrogel with and without 660 nm laser irradiation were determined. As shown in Fig. 4A, the plates of *S. aureus* colonies with different treatments, indicating that the composite hydrogel (PTCDs@Ag-AIPH) had obvious bactericidal effect under 660 nm laser irradiation. The antibacterial rate of the different Hydrogels against *S. aureus* was evaluated by counting colonies method. As depicted in Fig. 4B, all Hydrogel groups had basically no killing effect on bacteria without laser irradiation, and the viability rate of PTCDs Hydrogel group, PTCDs-AIPH Hydrogel group and PTCDs@Ag Hydrogel group were 90.62 %, 72.94 % and 9.97 % after laser irradiation, and that of PTCDs@Ag-AIPH Hydrogel group was all dead. The results showed that the prepared composite hydrogel (PTCDs@Ag-AIPH) had excellent bactericidal properties against *S. aureus* under laser irradiation. Moreover, the effect of free AIPH and Hydrogel@AIPH were also tested. As seen in Fig. S8, compared with control group, AIPH and Hydrogel@AIPH had no obvious antibacterial effect whether with or without laser. It could attribute to thermal responsiveness of AIPH, when without stimulation of therm, AIPH could not produce the alkyl free radical to inhibit the bacterial. Morphological changes and membrane damage of *S. aureus* under different treatments were observed by SEM (Fig. 4C). The bacteria treated with PTCDs@Ag-AIPH Hydrogel group still maintained a typical spherical shape with a complete and smooth surface, while the bacteria treated with PTCDs@Ag-AIPH Hydrogel + Laser group showed obvious perforation, which further demonstrated the antibacterial activity of laser on the composite hydrogel treatment system. Live/dead staining further verified the killing effect of different hydrogels on *S. aureus* (Fig. 4D). No obvious dead bacteria (green fluorescence, stained with SYTO9) were observed in the hydrogel group and the PTCDs@Ag-AIPH hydrogel group, regardless of laser irradiation. Due to the excellent antibacterial properties of PTCDs@Ag-AIPH hydrogel group, the bacteria were obviously killed (PI stained red fluorescence).

3.8. Anti-biofilm activity

To determine whether different groups of Hydrogel affected the biofilms that provided protection for microorganisms, extracorporeal therapy was performed using a representative *S. aureus* biofilm model. The killing effect of different hydrogels on the biofilm simulated by *S. aureus* with or without laser irradiation was shown in Fig. 5A. The antibacterial rate of the different Hydrogels against *S. aureus* biofilm was shown in Fig. 5B, all hydrogels had basically no killing effect on the biofilm of bacteria without laser irradiation. Under 660 nm laser irradiation, the survival rate of bacteria in PTCDs Hydrogel group was 97.12 %, that in PTCDS-AIPH Hydrogel group was 61.34 %, that in PTCDs@Ag Hydrogel group was 24.57 %, and the bacterial viability rate of PTCDs@Ag-AIPH Hydrogel group was 8.97 %, indicating that the prepared PTCDs@Ag-AIPH Hydrogel also had obvious bactericidal performance against *S. aureus* biofilm. Morphological changes and membrane damage of biofilm for PTCDs@Ag-AIPH Hydrogel were observed by SEM with or without laser irradiationwere (Fig. 5C). The biofilm treated with PTCDs@Ag-AIPH Hydrogel still maintained a typical spherical shape, while the biofilm treated with PTCDs@Ag-AIPH Hydrogel + Laser group showed obvious perforation, indicating its anti-biofilm activity under 660 nm laser irradiation. In Fig. 5D, the

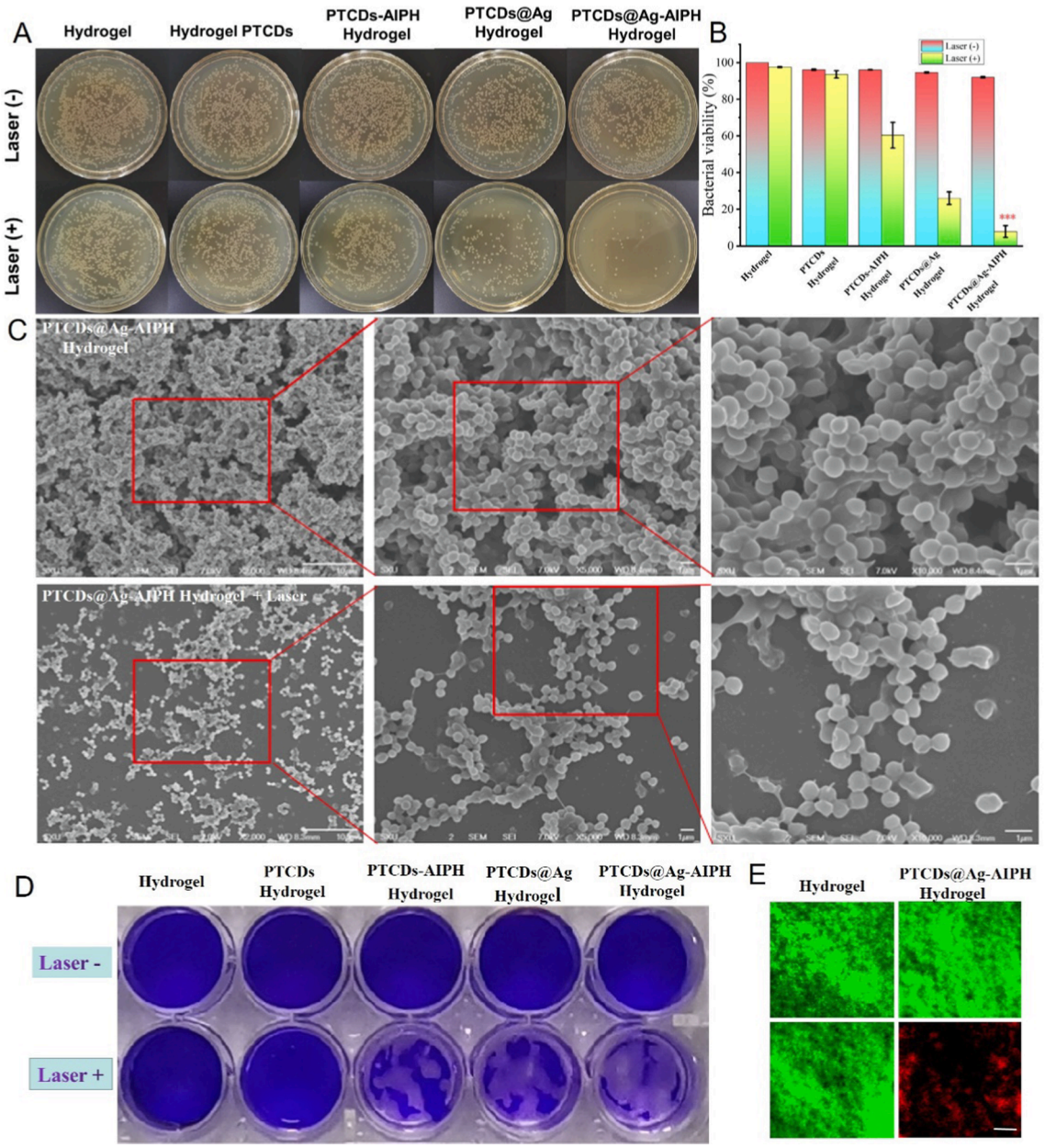

Fig. 5. (A) The plate photos of *S. aureus* biofilm cocultured with different Hydrogel groups with or without 660 nm laser irradiation. (B) The killing effect of the different Hydrogels against *S. aureus* biofilm (***P < 0.001, *vs* Hydrogel group); (C) The SEM images of *S. aureus* biofilm cocultured with PTCDs@Ag-AIPH Hydrogel with or without laser irradiation, Scale bar = 1 μm; (D) Microscopy images of crystal violet-stained *S. aureus* biofilms; (E) The specific killing effects of *S. aureus* biofilm with various treatments by live/dead staining. Scale bar = 20 μm.

antibiofilm abilities of different Hydrogel groups were determined by crystal violet staining method, manifesting that the PTCDs@Ag-AIPH Hydrogel + Laser group strongly inhibited the formation of biofilms. To further evaluate the antibiofilm activity, mature biofilms were grown on the small dish. The biofilms treated with Hydrogel control group and PTCDs@Ag-AIPH Hydrogel group were co-stained with SYTO9/PI. As seen in Fig. 5E, the viability and residual amounts of *S. aureus* in the biofilm could be quantitatively analyzed by CLSM, such as green fluorescent for alive and red for dead. The bacteria in the biofilm of Hydrogel, Hydrogel + Laser, PTCDs@Ag-AIPH Hydrogel group were mostly alive, while the bacteria in the biofilm of PTCDs@Ag-AIPH hydrogel + Laser group all died. These results indicated that the composite hydrogel had a strong killing effect on *S. aureus* biofilm after laser irradiation.

3.9. *In vivo antibiofilm and infected wound healing performances*

It was proved that the composite hydrogel had good antibacterial and antibiofilm properties *in vitro*, the ability to treat the biofilm-related wound infections mice was further explored. In order to better evaluate the effect of the prepared composite hydrogel on the treatment of the *S. aureus* biofilm-related wound infections, the low immunity modeling of mouse was carried out. Specifically, the mice were injected with cyclophosphamide twice 48 h apart in the abdominal cavity, and the blood was collected before and after the injection to test their white blood cell values, as shown in Fig. S9, the white blood cell value of the mice was normal before induction, which was 6.3×10^9/L. However, after induction, the white blood cell value decreased sharply, which was 0.8×10^9/L. The successful induction of immunocompromised mouse models were demonstrated. Before treatment, PTCDs@Ag-AIPH

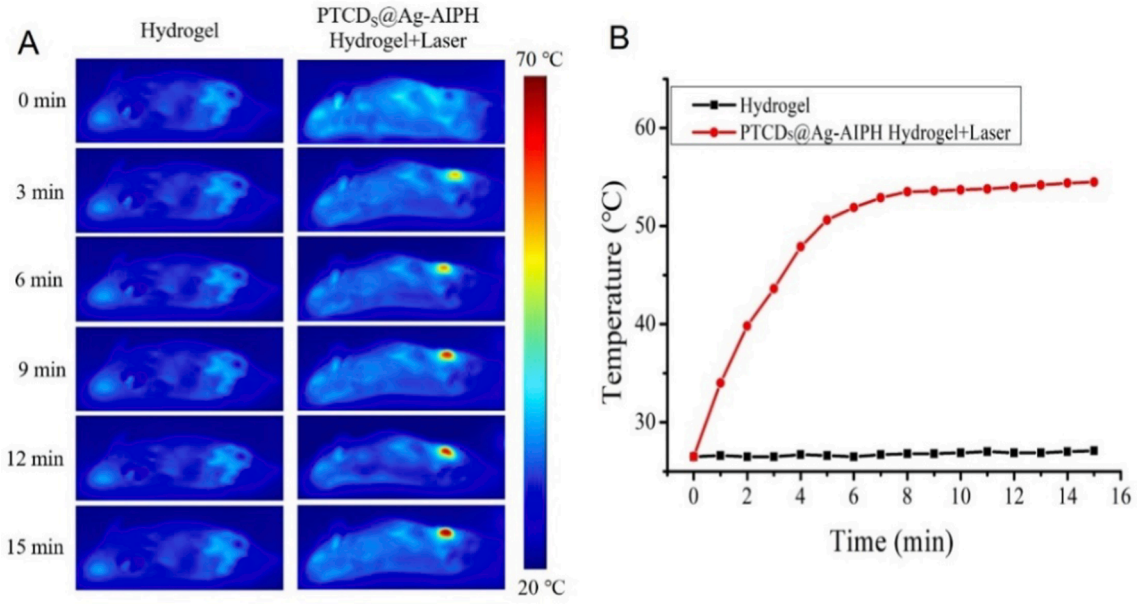

Fig. 6. (A) Thermal images of mice treated with Hydrogen and PTCDs@Ag-AIPH hydrogel under 660 nm laser irradiation for different time; (B) The corresponding photothermal temperature curves.

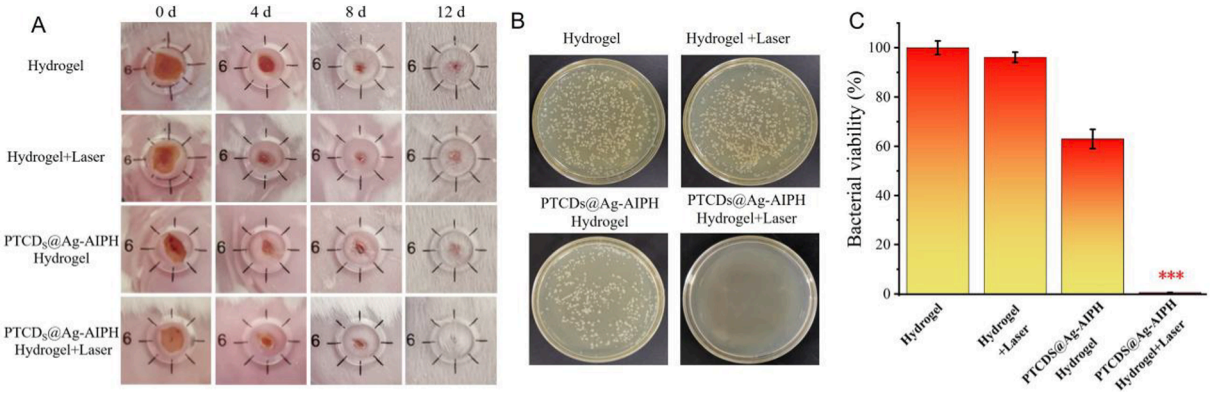

Fig. 7. Representative photographs of wound tissues treated with different Hydrogel groups under 660 nm laser irradiation or not. (B) Representative photographs and (C) The wound colony statistics of bacterial cultures taken from *S. aureus* infected wound areas during the treatment phase on day 12 (***P < 0.001, *vs* Hydrogel group).

hydrogel nanocomposites were introduced into the infected site to study the photothermal heating performances *in vivo*. As seen in Fig. 6A and Fig. 6B, after 15 min of irradiation, the wound temperature increased to 54.2 °C, which was higher than that of control Hydrogel treatment group, indicating a good PTT property of PTCDs@Ag-AIPH hydrogel nanocomposites.

Mice infected with *S. aureus* biofilms were then randomly assigned to the following four treatment groups on average. As shown in Fig. 7A, mice infected with *S. aureus* biofilms were then equally and randomly assigned to the four treatment groups. There were significant differences in the shape and size of the wounds among the treatment groups. The PTCDs@Ag-AIPH hydrogel + Laser group exhibited the smallest wound area after 12 days of treatment for comparing with other treatment groups. However, the wound healing trend of hydrogel control group and hydrogel + laser group was not obvious, and the skin injury was more serious. These results showed that PTCDs@Ag-AIPH hydrogel had good antibacterial and anti-biofilm properties, which was in good agreement with the results of *in vitro* antibacterial and anti-biofilm experiments. Local bacteria on the wound of each group were collected, and the antibacterial effect of each hydrogel group *in vivo* was quantitatively analyzed (Fig. 7B). The number of bacteria on the wound after treatment with PTCDs@Ag-AIPH hydrogel + Laser was significantly lower than that in other groups. Statistical analysis of wound colonies was also consistent with these results (Fig. 7C), indicating that PTCDs@Ag-AIPH hydrogel had potential bactericidal and biofilm-killing and promoted wound healing effects *in vivo*. To evaluate the biosafety and wound recovery of different treatment groups, hematoxylin and eosin (H&E) staining were performed on major organs and original wound healing skin. H&E staining was performed on heart, liver, lung and kidney, no histopathological abnormalities of different group were found from Fig. S10, these results strongly suggested that the proposed hydrogel nanocomposite were safe in mammals and had great potential for the efficient treatment of biofilm-associated wound infections. Meanwhile, after 12 days of treatment, wound tissue from each mouse was collected and analyzed with H&E staining. As seen in Fig. S10, the control group still had severe inflammatory cell infiltration, indicating serious bacterial infection, in PTCDs@Ag-AIPH hydrogel + Laser group, the infiltration of inflammatory cells in the wound tissues had significant decrease.

4. Conclusion

In summary, the novel multi-functional carbon dots (PTCDs) which emitted red fluorescence and had good photothermal properties were synthesized. The photothermal-triggered injectable Hydrogel (PTCDs@Ag-AIPH Hydrogel) was successfully developed by loading PTCDs@Ag and thermal-labile AIPH initiator into gelatin, which overcomed the disadvantage that traditional hydrogels could not cover irregular wounds and had good biosafety. Under the irradiation of 660 nm laser, the hydrogel generated heat for sterilization, the generated heat could melt the hydrogel for releasing Ag^+ and activated AIPH to release alkyl free radical sterilization. *In vitro* and *in vivo* experiments showed that PTCDs@Ag-AIPH Hydrogel had a strong destructive effect on *S. aureus* and its biofilm, which provided a potential therapeutic means for clinical bacterial infection-related diseases.

CRediT authorship contribution statement

Wen Liu: Conceptualization, Data curation, Funding acquisition, Methodology, Writing – original draft, Writing – review & editing. **Baizhi Su:** Conceptualization, Data curation, Methodology, Writing – review & editing. **Hua Song:** Formal analysis, Investigation, Writing – review & editing. **Xueyun Zhang:** Conceptualization, Data curation, Methodology. **Guodong Ren:** Data curation, Methodology, Writing – review & editing. **Xuewei Wang:** Conceptualization, Resources. **Lili Yan:** Funding acquisition, Supervision. **Sufang Ma:** Investigation, Supervision. **Lihong Li:** Resources, Supervision. **Lixia Guo:** Conceptualization, Methodology, Supervision, Writing – review & editing. **Shuming Xu:** Methodology, Supervision, Writing – review & editing. **Boye Zhang:** Conceptualization, Methodology. **Haipeng Diao:** Funding acquisition, Resources, Supervision. **Zhifang Wu:** Conceptualization, Resources, Writing – review & editing. **Sijin Li:** Conceptualization, Resources. **Chengwu Zhang:** Conceptualization, Investigation, Methodology, Writing – review & editing.

Declaration of competing interest

The authors declare that they have no known competing financial interests or personal relationships that could have appeared to influence the work reported in this paper.

Acknowledgements

We appreciate the financial support from the National Nature Science Foundation of China (82071969, 82202289), the Natural Science Foundation of Shanxi Province (202203021211236, 20210302123294, 202103021224436, 20210302124341, 20210302123299, 202203021212375) and Yingze District Science and Technology Project of Taiyuan City (2022).

Appendix A. Supplementary data

Supplementary data to this article can be found online at https://doi.org/10.1016/j.arabjc.2024.105755.

References

Bao, L., Zhang, Z., Tian, Z., Zhang, L., Liu, C., Lin, Y., Qi, B., Pang, D., 2011. Electrochemical tuning of luminescent carbon nanodots: from preparation to luminescence mechanism. Adv. Mater. 23, 5801–5806.

Bastien, S., Meyers, S., Salgado-Pabón, W., Giulieri, S.G., Rasigade, J.P., Liesenborghs, L., Kinney, K.J., Couzon, F., Martins-Simoes, P., Moing, V.L., Duval, X., Holmes, N.E., Bruun, N.E., Skov, R., Howden, B.P., Fowler Jr., V.G., Verhamme, P., Andersen, P.S., Bouchiat, C., Moreau, K., Vandenesch, F., 2023. All *Staphylococcus aureus* bacteraemia-inducing strains can cause infective endocarditis: results of GWAS and experimental animal studies. J. Infect. 86, 123–133.

Chen, Z., Shan, J., Niu, Q., Chen, H., Zhang, W., Cao, D., Wang, X., 2024. pH-responsive double-enzyme active metal-organic framework for promoting the healing of infected wounds. J. Colloid Interf. Sci. 657, 250–262.

Cui, Y., Zhang, W., Shan, J., He, J., Niu, Q., Zhu, C., Wang, W., Chen, X.L., Wang, X., 2023. Copper nanodots-based hybrid hydrogels with multiple enzyme activities for acute and infected wound repair. Adv. Healthc, Mater, p. 2302566.

Das, P., Bose, M., Das, A.K., Banerjee, S., Das, N.C., 2018. One-step synthesis of fluorescent carbon dots for bio-labeling assay. Macromol. Sym. 382, 1–6.

Dieltjens, L., Appermans, K., Lissens, M., Lories, B., Kim, W., Eycken, E.V., Foster, K.R., Steenackers, H.P., 2020. Inhibiting bacterial cooperation is an evolutionarily robust anti-biofilm strategy. Nat. Commun. 11, 107.

Dong, Y.H., Wang, L.P., Burgner, D.P., Miller, J.E., Song, Y., Ren, X., Li, Z.J., Xing, Y., Ma, J., Sawyer, S.M., Patton, G.C., 2020. Infectious diseases in children and adolescents in China: analysis of national surveillance data from 2008 to 2017. BMJ 369, m1043.

Geng, B., Yan, L., Zhu, Y., Shi, W., Wang, H., Mao, J., Ren, L., Zhang, J., Tian, Y., Gao, F., Zhang, X., Chen, J., Zhu, J., 2023. Carbon Dot@MXene nanozymes with triple enzyme-mimic activities for mild NIR-II photothermal-amplified nanocatalytic therapy. Adv. Healthc. Mater. 12, 2202154.

He, H., Fei, Z., Guo, T., Hou, Y., Li, D., Wang, K., Ren, F., Fan, K., Zhou, D., Xie, C., Wang, C., Lu, X., 2022. Bioadhesive injectable hydrogel with phenolic carbon quantum dot supported pd single atom nanozymes as a localized immunomodulation niche for cancer catalytic immunotherapy. Biomaterials 280, 121272.

Jin, X., Shan, J., Zhao, J., Wang, T., Zhang, W., Yang, S., Qian, H., Cheng, L., Chen, X., Wang, X., 2024. Bimetallic oxide cu-Fe_3O_4 nanoclusters with multiple enzymatic activities for wound infection treatment and wound healing. Acta Biomater. 173, 403–419.

Jin, J., Wang, B., Xu, Z., He, X., Zou, H., Yang, Q., Jiang, F., Liu, Y., 2018. A novel method for the detection of silver ions with carbon dots: excellent selectivity, fast response, low detection limit and good applicability. Sens. Actuators B Chem. 267, 627–635.

Kawabe, Y., Sakurai, A., Sasaki, T., Hasegawa, M., Suzuki, M., Hoshino, N., Nakashima, C., Maekawa, A., Doi, Y., 2022. Native valve infective endocarditis due to sequence type 97 community-associated methicillin-resistant Staphylococcus aureus complicated by meningitis and multiple septic emboli in a young healthy adult. J. Infect. Chemother. 28, 828–832.

Li, H., Yang, K., Hai, L., Wang, Z., Luo, Y., He, L., Yi, W., Li, J., Xu, C., Deng, L., He, D., 2023. Photothermal-triggered release of alkyl radicals and cascade generation of hydroxyl radicals via a versatile hybrid nanocatalyst for hypoxia-irrelevant synergistic antibiofilm therapy. Chem. Eng. J. 455, 140903.

Lin, J., Li, Y., Wang, P., Wu, M., Zhu, F., Zhang, Y., Hou, Z., Liu, J., Liu, X., 2022. Natural killer cell membrane-cloaked virus-mimicking nanogenerator with NIR-triggered shape reversal and ·C/·OH storm for synergistic thermodynamic-chemodynamic therapy. Adv. Sci. 9, 2103498.

Liu, M., Huang, L., Xu, X., Wei, X., Yang, X., Li, X., Wang, B., Xu, Y., Li, L., Yang, Z., 2022a. Copper doped carbon dots for addressing bacterial biofilm formation, wound infection, and tooth staining. ACS Nano 16, 9479–9497.

Liu, W., Li, J., Wang, Z., Tian, Y., Ren, G., Hou, X., Guo, L., Li, L., Zhang, C., Wu, Z., Yan, L., Li, S., Diao, H., 2022b. Construction of mitochondria targeted and fret based ratiometric sensing nanoplatform for sulfur dioxide accurate detection *in vitro* and *in vivo*. Spectrochim. Acta A 283, 121731.

Long, L., Ge, Z., Zhang, F., Dong, R., Yang, L., Chen, Z., Tang, S., Wang, Y., 2023. Development of injectable hyaluronic acid-based hydrogels with antioxidant activity for the treatment of corneal neovascularization. Chem. Eng. J. 478, 147147.

Lu, Y., Zhao, M., Peng, Y., He, S., Zhu, X., Hu, C., Xia, G., Zuo, T., Zhang, X., Yun, Y., Zhang, W., Shen, X., 2022. A physicochemical double-cross-linked gelatin hydrogel with enhanced antibacterial and anti-inflammatory capabilities for improving wound healing. J. Nanobiotechnol. 20, 426.

Mah, T.F., O'Toole, G.A., 2001. Mechanisms of biofilm resistance to antimicrobial agents. Trends in Microbiol. 9, 34–39.

Maria, X., Mehrdad, R., Petros, M., Anthony, M., Shideh, T., Marco, B., Beatrice, P., Neil, L., 2023. A double-crosslinked nanocellulose-reinforced dexamethasone-loaded collagen hydrogel for corneal application and sustainedanti-inflammatory activity. Acta Biomater. 172, 234–248.

Mukherjee, S., Bassler, B.L., 2019. Bacterial quorum sensing in complex and dynamically changing environments. Nat. Rev. Microbiol. 17, 371–382.

Nies, L., Kobras, C.M., Stracy, M., 2023. Antibiotic-induced collateral damage to the microbiota and associated infections. Nat. Rev. Microbiol. 21, 789–804.

Nugroho, D., Thinthasit, A., Khoris, I.M., Siriputthaiwan, P., Benchawattananon, R., Chanthai, S., 2024. L-histidine doped CDs from zingiber montanum using hydrothermal method to enhance its antimicrobial activity and imply for latent fingerprint detection. Arabian J. Chem. 17, 105602.

Rajasekar, S., Martin, E.M., Kuppusamy, S., Vetrivel, C., 2020. Chitosan coated molybdenum sulphide nanosheet incorporated with tantalum oxide nanomaterials for improving cancer photothermal therapy. Arabian J. Chem. 11 (3), 4741–4750.

Rello, J., Campogiani, L., Eshwara, V.K., 2019. Understanding resistance in enterococcal infections. Intens. Care Med. 46, 353–356.

Ren, G., Wang, Z., Tian, Y., Li, J., Ma, Y., Zhou, L., Zhang, C., Guo, L., Diao, H., Li, L., Lu, L., Ma, S., Wu, Z., Yan, L., Liu, W., 2022. Targeted chemo-photodynamic therapy toward esophageal cancer by GSH-sensitive theranostic nanoplatform. Biomed. Pharmacother. 153, 113506.

Rumbaugh, K.P., Sauer, K., 2020. Biofilm dispersion. Nat. Rev. Microbiol. 18, 571–586.

Shan, J., Jin, X., Zhang, C., Huang, M., Xing, J., Li, Q., Cui, Y., Niu, Q., Chen, X., Wang, X., 2024. Metal natural product complex Ru-procyanidins with quadruple enzymatic activity combat infections from drug-resistant bacteria. Acta Pharm. Sin. B. https://doi.org/10.1016/j.apsb.2023.12.017.

Shen, Y., Nie, C., Pan, T., Zhang, W., Yang, H., Ye, Y., Wang, X., 2023. A multifunctional cascade nanoreactor based on Fe-driven carbon nanozymes for synergistic photothermal/chemodynamic antibacterial therapy. Acta Biomater. 168, 580–592.
Song, Y., Yan, X., Li, Z., Qu, L., Zhu, C., Ye, R., Li, S., Du, D., Lin, Y., 2018. Highly photoluminescent carbon dots derived from linseed and their applications in cellular imaging and sensing. J. Mater. Chem. B 6, 3181–3187.
Stubbe, B., Mignon, A., Damme, L., Claes, K., Hoeksema, H., Monstrey, S., Vlierberghe, S., Dubruel, P., 2021. Photo-crosslinked gelatin-based hydrogel films to support wound healing. Macromol. Biosci. 21, 2100246.
Sun, Y., Zhou, B., Lin, Y., Zhou, B., Lin, Y., Wang, W., Wang, X., Wang, H., 2006. Quantum-sized carbon dots for bright and colorful photoluminescence. J. Am. Chem. Soc. 128, 7756–7757.
Wan, X., Xiao, J., Yin, M., Yao, Y., Luo, J., 2023. Counterion-induced antibiotic-based small-molecular micelles for methicillin-resistant Staphylococcus aureus infections. Acta Biomater. 166, 627–639.
Wang, L., Niu, X., Song, Q., Jia, J., Hao, Y., Zheng, C., Ding, K., Xiao, H., Liu, X., Zhang, Z., Zhang, Y., 2020. A two-step precise targeting nanoplatform for tumor therapy via the alkyl radicals activated by the microenvironment of organelles. J. Control. Release 318, 197–209.
Willyard, C., 2017. The drug-resistant bacteria that pose the greatest health threats. Nature 543, 15.
Yang, S., Chen, Z., Zhou, P., Xia, J., Deng, T., Yu, C., 2023. Carbon dots based on endogenous nutrients with visible and nir fluorescence to penetrate blood-brain barrier. Carbon 202, 130–140.
Yu, X., He, D., Zhang, X., Zhang, H., Song, J., Shi, D., Fan, Y., Luo, G., Deng, J., 2019. Surface adaptive and initiator-loaded graphene as a light-induced generator with free radicals for drug-resistant bacteria eradication. ACS Appl. Mater. Inter. 11, 1766–1781.
Zhao, Y., Wang, D., Oian, T., Zhang, J., Li, Z., Gong, Q., Ren, X., Zhao, Y., 2023. Biomimetic nanozyme-decorated hydrogels with H_2O_2-activated oxygenation for modulating immune microenvironment in diabetic wound. ACS Nano 17, 16854–16869.
Zhou, Z., Deng, T., Tao, M., Lin, L., Sun, L., Song, X., Gao, D., Li, J., Wang, Z., Wang, X., Li, J., Jiang, Z., Luo, L., Yang, L., Wu, M., 2023. Snail-inspired AFG/GELMA hydrogel accelerates diabetic wound healing viainflammatory cytokines suppression and macrophage polarization. Biomaterials 299, 122141.